A search for R-parity-violating supersymmetry in final states containing many jets in $\sqrt{s} = 13\,\text{TeV}$ pp collisions with the ATLAS detector

The ATLAS Collaboration

A search for R-parity-violating supersymmetry in final states with high jet multiplicity is presented. The search uses $140\,\text{fb}^{-1}$ of $\sqrt{s} = 13\,\text{TeV}$ proton–proton collision data collected by the ATLAS experiment during Run 2 of the Large Hadron Collider. The results are interpreted in the context of R-parity-violating supersymmetry models that feature prompt gluino-pair production decaying directly to three jets each or decaying to two jets and a neutralino which subsequently decays promptly to three jets. No significant excess over the Standard Model expectation is observed and exclusion limits at the 95% confidence level are extracted. Gluinos with masses up to 1800 GeV are excluded when decaying directly to three jets. In the cascade scenario, gluinos with masses up to 2340 GeV are excluded for a neutralino with mass up to 1250 GeV.
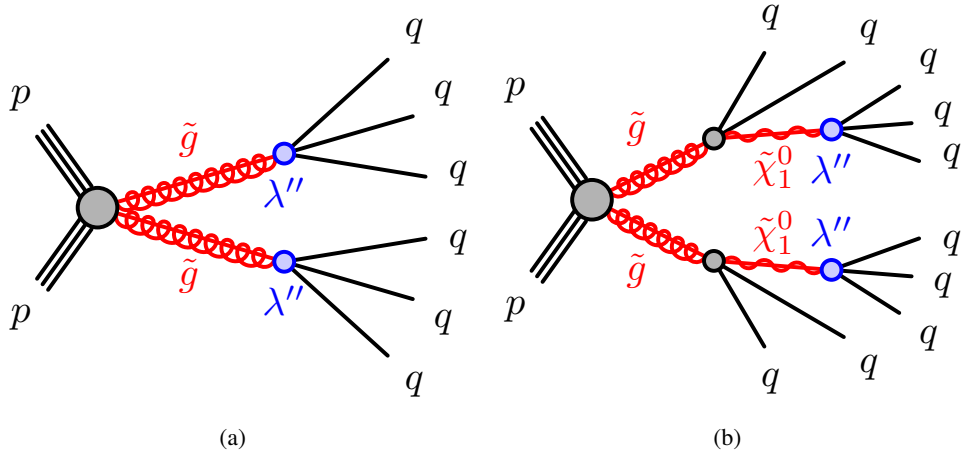
Figure 1: Signal diagrams for the gluino direct decay model (left) and gluino cascade decay model (right) targeted in this analysis.

1 Introduction

Supersymmetry (SUSY) [1–6] is a theoretical extension of the Standard Model (SM) which fundamentally relates fermions and bosons by introducing a partner particle for each SM particle. It is an alluring theoretical possibility given its potential to solve the hierarchy problem [7–10]. An ad-hoc conserved quantity, R-parity [11], is often introduced in SUSY models to avoid rapid proton decay, rendering the lightest supersymmetric particle (LSP) stable and therefore a potential dark-matter candidate [12, 13]. However, there is no fundamental theoretical reason to impose strict R-parity conservation. R-parity-violating (RPV) SUSY models are well motivated and generally have fewer experimental constraints than many R-parity-conserving (RPC) models [14, 15]. This suggests that the ATLAS Run 2 dataset could contain thousands of events where the supersymmetric partner of the gluon, the gluino ($\tilde{g}$) is present.

This article presents a search for supersymmetric gluinos ($\tilde{g}$) pair production with subsequent RPV decays into quarks in events with many jets using 140 fb^{-1} of pp collision data collected at $\sqrt{s} = 13$ TeV by the ATLAS detector during Run 2 of the LHC. Such a final state is predicted in RPV models with a non-zero baryon-number-violating $U\bar{D}\bar{D}$ coupling [16, 17]. The dominant SM background process originates from multi-jet production, with a cross-section multiple orders of magnitude higher than the targeted signals. Two approaches are implemented to distinguish between the SM background and potential SUSY signal. The first, so-called "jet counting" analysis defines several search regions requiring many high p_T jets. The background is estimated using a combination of both data and simulation, where events containing low jet multiplicities and low momenta are extrapolated to higher jet-momenta and multiplicities. The second, "mass resonance", approach aims to reconstruct the gluino mass with machine-learning methods, solving the combinatorial assignment challenge to correctly identify which jets belong to a given gluino. A mass-resonance search is then performed on the gluino-candidate mass spectrum. A fully data-driven approach is used to estimate the background, with a functional fit of the smoothly falling gluino-candidate mass distribution.

Two RPV SUSY simplified signal models [18–20] featuring gluino-pair production are targeted. Figure 1(a) presents the gluino direct-decay model, where the gluino decays into three quarks via a $\lambda''_{ijk} U\bar{D}\bar{D}$ RPV coupling, leading to final states containing at least six jets. The gluino cascade-decay model is presented in

2

Figure 1(b), in which the gluino decays to two quarks and neutralino, $\tilde{\chi}_1^0$, where the neutralinos result from the mixing between the supersymmetric partners of the neutral SM bosons. The neutralino then decays into three quarks, again via the λ''_{ijk} $U\bar{D}\bar{D}$ coupling, leading to at least ten jets in the final state. Both scenarios assume that λ''_{ijk} is large enough to ensure prompt SUSY decays. Two couplings are considered, λ''_{112} and λ''_{113}, leading to the RPV decays $\tilde{g}/\tilde{\chi}_1^0 \to uds$ referred to as the UDS-decay or $\tilde{g}/\tilde{\chi}_1^0 \to udb$ referred to as the UDB-decay respectively. The results of this note apply equally to other couplings, λ''_{ij2}, λ''_{ij3}, with $i, j \in 2, 3$, since it leads to the same experimental final state. The UDB-decay leads to a unique signal phenomenology containing bottom quarks and a dedicated event selection containing b-tagged jets is employed to specifically target this scenario.

Previous searches in this final state have been performed by the ATLAS [21, 22] and CMS collaborations [23]. This analysis uses new methods in both the jet counting and mass resonance approaches, dramatically improving the sensitivity beyond the expected gains due to the larger dataset.

2 ATLAS detector

The ATLAS experiment [24] at the LHC is a multipurpose particle detector with a forward–backward symmetric cylindrical geometry and a near 4π coverage in solid angle.[1] It consists of an inner tracking detector surrounded by a thin superconducting solenoid providing a 2 T axial magnetic field, electromagnetic and hadron calorimeters, and a muon spectrometer. The inner tracking detector covers the pseudorapidity range $|\eta| < 2.5$. It consists of silicon pixel, silicon microstrip, and transition radiation tracking detectors. Lead/liquid-argon (LAr) sampling calorimeters provide electromagnetic (EM) energy measurements with high granularity. A steel/scintillator-tile hadron calorimeter covers the central pseudorapidity range ($|\eta| < 1.7$). The endcap and forward regions are instrumented with LAr calorimeters for both the EM and hadronic energy measurements up to $|\eta| = 4.9$. The muon spectrometer surrounds the calorimeters and is based on three large superconducting air-core toroidal magnets with eight coils each. The field integral of the toroids ranges between 2.0 and 6.0 T m across most of the detector. The muon spectrometer includes a system of precision tracking chambers and fast detectors for triggering. A two-level trigger system is used to select events. The first-level trigger is implemented in hardware and uses a subset of the detector information to accept events at a rate below 100 kHz. This is followed by a software-based trigger that reduces the accepted event rate to 1 kHz on average depending on the data-taking conditions. An extensive software suite [25] is used in data simulation, in the reconstruction and analysis of real and simulated data, in detector operations, and in the trigger and data acquisition systems of the experiment.

3 Data and simulated event samples

The data analysed in this paper were collected between 2015 and 2018 at a centre-of-mass energy of 13 TeV with a 25 ns proton bunch crossing interval. The average number of pp interactions per bunch crossing, referred to as pile-up, ranged from 13 in 2015 to around 38 in 2017–2018. Application of beam, detector and data-quality criteria [26] results in a total integrated luminosity of 140 fb^{-1}.

---

[1] ATLAS uses a right-handed coordinate system with its origin at the nominal interaction point (IP) in the centre of the detector and the z-axis along the beam pipe. The x-axis points from the IP to the centre of the LHC ring, and the y-axis points upwards. Polar coordinates (r, ϕ) are used in the transverse plane, ϕ being the azimuthal angle around the z-axis. The pseudorapidity is defined in terms of the polar angle θ as $\eta = -\ln\tan(\theta/2)$. Angular distance is measured in units of $\Delta R \equiv \sqrt{(\Delta\eta)^2 + (\Delta\phi)^2}$.

Monte Carlo (MC) samples are primarily used in the analysis to estimate the expected number of events for a given signal scenario. MC samples are also used to aid in the modelling of the SM backgrounds in the search regions, or as a cross-check of the data-driven methods used to model the expected background yield.

Signal samples are generated at leading-order (LO) accuracy with up to two additional partons using the MadGraph5_aMC@NLO event generator [27] interfaced with Pythia8 [28]. The A14 [29] set of tunes are used for underlying event together with the NNPDF2.3LO [30] parton distribution function (PDF) set. The EvtGen program [31] is used to generate the events in free space which is then passed through a simulated version of the ATLAS detector using GEANT4 [32, 33]. The signal cross-sections are calculated at next-to-next-to-leading order (NNLO) in the strong coupling constant, adding the resummation of soft gluon emission at next-to-next-to-leading-logarithmic accuracy (NNLO+NNLL).

Multijet events constitute the dominant background in the search region. Multijet production in the SM is generated using Pythia 8.230 [34] with leading-order matrix elements for dijet production which are matched to the parton shower. The renormalisation and factorisation scales are set to the geometric mean of the squared transverse masses of the two outgoing particles in the matrix element. The NNPDF2.3LO PDF set is used in the ME generation, the parton shower, and the simulation of the multi-parton interactions. The A14 set of tuned parameters is used. Perturbative uncertainties are estimated through event weights [28] that encompass variations of the scales at which the strong coupling constant is evaluated in the initial- and final-state shower as well as the PDF uncertainty in the shower and the non-singular part of the splitting functions.

In the regions requiring the presence of a jet identified as originating from a b-quark, there is contribution from top-quark pair production ($t\bar{t}$). The production of fully hadronic decays of $t\bar{t}$ events, is modeled at NLO using the Powheg Box [35, 36] generator. Additional $t\bar{t}$ samples are generated with MadGraph5_aMC@NLO interfaced with Pythia 8, and with Powheg Box interfaced with Herwig 7 [37, 38], for the evaluation of systematic uncertainties.

The effect of pile-up interactions is modelled by overlaying the simulated hard-scattering event with inelastic proton–proton (pp) events generated with Pythia 8.186 [39] using the NNPDF2.3LO set of parton distribution functions (PDF) [30] and the A3 set of tuned parameters [40].

The Monte Carlo (MC) events are weighted to reproduce the distribution of the average number of interactions per bunch crossing ($\langle\mu\rangle$) observed in the data. The $\langle\mu\rangle$ value in data is rescaled by a factor of 1.03 ± 0.04 to improve agreement between data and simulation in the visible inelastic proton–proton (pp) cross-section [41].

4 Event Reconstruction

As the signal scenarios under investigation have a general event phenomenology consisting of a large number of energetic jets, an identical trigger strategy and a set of common object definitions can be used for both analysis strategies.

Events are required to pass an H_{T} trigger, which is the scalar sum of the transverse energy of the jets in the event. To ensure the trigger is fully efficient, a selection of $H_{\mathrm{T}} > 1100\,\mathrm{GeV}$ and a selection on the transverse momentum of the leading jet, $p_{\mathrm{T}}(j_1) > 200\,\mathrm{GeV}$, is applied. The H_{T} trigger has an efficiency exceeding 95% for signal events passing the selection for all data-taking periods.

Jets are reconstructed using the particle flow (PFlow) algorithm [42], which suppresses calorimeter energy deposits arising from charged pileup particles and takes the momentum estimation from tracks whenever the tracker resolution is better than the calorimeter resolution. The anti-k_T algorithm [43] with a size parameter of $R = 0.4$ is subsequently used to define the analysis-level jets. Jets containing a large particle momentum contribution from pile-up vertices, as measured by the jet vertex tagger (JVT) discriminant [44] are rejected if they have $p_T \in [20, 60]$ GeV, $|\eta| < 2.4$ and a discriminant value of JVT < 0.5. Two classes of jets are defined: "baseline" jets and "signal" jets. Baseline jets require $p_T > 20$ GeV and $|\eta| < 4.8$. Signal jets are used for the computation of kinematic variables and for the final event selections and require $p_T > 50$ GeV and $|\eta| < 2.8$.

Selected jets are tagged as b-jets if they are within the inner tracking detector acceptance of $|\eta| < 2.5$ and are identified by a multivariate algorithm (DL1r) which uses a selection of inputs including information about the impact parameters of inner detector tracks, the presence of displaced secondary vertices and the reconstructed flight paths of b- and c-hadrons inside the jet [45]. The b-tagging algorithm uses a working point with an efficiency of 77%, determined with a sample of simulated $t\bar{t}$ events. The corresponding misidentification (mis-tag) rate is 20% for c-jets and 0.9% for light-flavour jets. Differences in efficiency and mis-tag rate between data and MC simulation are taken into account with correction factors as described in Ref.[45].

As the signal scenarios considered do not contain any light leptons (e, μ) signal sensitivity can be increased by vetoing events containing leptons. Electron candidates are reconstructed from an isolated electromagnetic calorimeter energy deposit matched to an inner detector track [46] and are required to possess $p_T > 10$ GeV and $|\eta| < 2.47$, and to satisfy the "Loose" likelihood-based identification criteria described in Refs.[46, 47]. Muon candidates are formed by combining information from the muon spectrometer and inner detector as described in Ref.[48] and are required to possess $p_T > 10$ GeV and $|\eta| < 2.7$. Furthermore, muon candidates must satisfy the "Medium" identification requirements described in Ref.[48]. In both cases lepton candidates must additionally have a longitudinal impact parameter relative to the primary vertex $|z_0 \sin\theta| < 0.5$ mm.

Multiplicative scale factors are applied to simulated events to account for differences between data and simulation for reconstruction, identification and isolation efficiencies, for example to account for the jet momentum scales and energy resolutions. Similar corrections are also applied to the probability of mis-tagging jets originating from the hard scattering as pile-up jets with the JVT discriminant, and the associated corrections related to the efficiency of identifying jets arising from b-hadrons.

After the object selection step, a procedure to avoid double counting of tracks and energy depositions associated with overlapping reconstructed jets, electrons, and muons is implemented. This procedure applies the following actions to the baseline jets and leptons in a sequential order. If a jet and an electron are within $\Delta R = \sqrt{(\Delta\eta)^2 + (\Delta\phi)^2} < 0.2$ the jet is removed, whereas if jet and an electron are within $\Delta R < 0.4$ the electron is removed. If a jet and a muon are within $\Delta R < 0.2$, or the muon track is associated with the jet, the jet is removed if the number of tracks is fewer than three and if the jet and total track p_T is consistent with the muon energy. Finally if a muon and a jet are within $\Delta R < 0.4$ the muon is rejected.

5 Analysis Strategy

The signal scenarios considered are targeted using two complementary analysis methods. In addition to possessing common object and trigger requirements, similar kinematic variables are employed to perform

a simple discrimination between signal and background, upon which the two analyses build upon.

Events are required to pass the H_T trigger, and all of the associated requirements to assure the trigger is fully efficient as discussed in Section 4. All events veto the presence of any leptons (e, μ), and are required to contain at least four jets with $p_T > 50\,\text{GeV}$.

For both analyses, the event-shape variable C [49] derived from the linearized sphericity tensor of the event is used to distinguish between signal and background. The sphericity tensor, which captures the momentum distributions of an event, can be reduced to three eigenvalues, $\lambda_1, \lambda_2, \lambda_3$, representing the shape of this distribution along three orthogonal directions. It is calculated as a combination of these eigenvalues as:

$$C = 3(\lambda_1\lambda_2 + \lambda_1\lambda_3 + \lambda_2\lambda_3) \tag{1}$$

For events consisting of two back-to-back jets, which dominate the QCD multi-jet background, the C value tends to be smaller than for gluino decays where the energy is distributed more uniformly or isotropically and the C value tends to larger values. A selection on the C variable and a selection requiring many high-p_T jets are employed by both analysis methods, as key variables to discriminate between the signal and the SM background. Figure 2 presents unit-area-normalised comparisons of these key variables, showing the significant differences between the signal models and the background.

The following two sections describe the signal optimisation strategy and the background estimation methods for the *jet counting analysis*, and the *mass resonance analysis* respectively. While both analyses target the direct decay scenario, the jet counting analysis provides a more model-independent approach which could see a general excess in events with large jet multiplicities and also investigates the cascade decay scenario, the mass resonance analysis is more model specific, and focuses specifically on the direct decay scenario, seeking to reconstruct the gluino mass directly from the decay products.
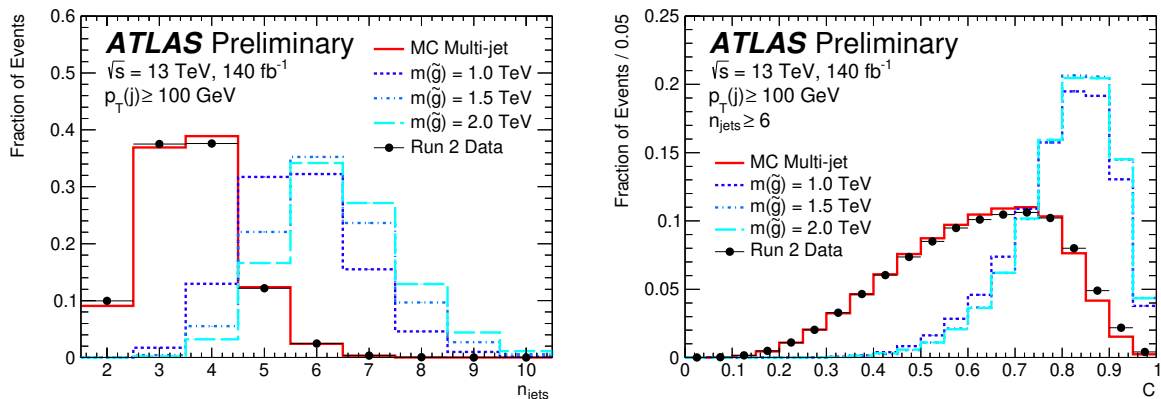
Figure 2: Comparison between normalised to unity distributions of the observed data, the QCD Multi-jet background and signal models. Left: n_{jets} spectrum with a p_T requirement of 100 GeV. Right: distribution of the C variable for events with at least 6 jets above 100 GeV.

5.1 Jet counting analysis

The *jet counting analysis* is built on the fact that the signal scenarios considered produce a large multiplicity of high-p_T jets, a feature that has been already exploited in previous analyses targeting similar models [21, 50]. In this approach, signal regions (SRs) are defined by requiring a high jet multiplicity and a tight

requirement on the p_T of the jets. The expected number of background events in this region is estimated by using control regions (CRs) which are defined with lower jet p_T requirements, which are then extrapolated to the SRs. To check the validity of this extrapolation, the background expectation (extrapolated from the CR) is compared to the observed data in intermediate validation regions (VRs), which are tighter than the CR requirements, but looser than the SRs.

In total seven SRs are defined to target different regions of the SUSY phase space under consideration. The SRs are sensitive to both the direct gluino decay scenario and for the cascade scenario. Table 1 presents the SR selections. All SRs require at least seven high p_T jets, and tight selections on the C variable. A selection of at least seven jets is chosen, instead of six as suggested by the tree-level diagrams, as the inclusion an extra jet which arises from initial or final state radiation is found to increase the sensitivity to the signal scenarios and further reject background events. Two SRs are defined with a requirement on the number of b-tagged jets present to specifically target the scenarios where the UDB-coupling allows for b-quarks in the decay.

Table 1: SR definitions for the jet counting method, n_{jets} represents the number of jets above the given p_T threshold ($p_T(j)$). The common analysis selections on the H_T, $p_T(j_1)$ and trigger selection are also applied.

	n_{jets}	$p_T(j)$ [GeV]	C	$n_{b-\text{jets}}$
SR1	≥ 7	180	≥ 0.90	-
SR2	≥ 7	220	≥ 0.90	-
SR3	≥ 7	240	≥ 0.90	-
SR4	≥ 8	180	≥ 0.85	-
SR5	≥ 8	210	≥ 0.85	-
SR1bj	≥ 7	180	≥ 0.85	≥ 2
SR2bj	≥ 8	180	≥ 0.85	≥ 2

Background estimation method

The primary source of background arises from QCD multi-jet events, which are estimated using a semi-data-driven approach. Multi-jet MC is employed to compute transfer factors across different jet multiplicities, while the prediction is normalised using data. The number of expected events with a given jet multiplicity n_{jets} above a certain jet-p_T threshold X (denoted as N_{n,p_T^X}) can be evaluated as:

$$N_{i,p_T^X} = w_i \cdot N_{4,p_T^X}^{\text{Data}} \cdot \frac{N_{i,p_T^X}^{\text{MC}}}{N_{4,p_T^X}^{\text{MC}}}$$

$$w_i = \frac{N_{i,p_T^{60}}^{\text{Data}}}{N_{i,p_T^{60}}^{\text{MC}}} \Bigg/ \frac{N_{4,p_T^{60}}^{\text{Data}}}{N_{4,p_T^{60}}^{\text{MC}}} \qquad (2)$$

$$N_{\geq n,p_T^X} = \sum_{i=n}^{n+2} N_{i,p_T^X}$$

To address potential biases in the MC modeling of the jet multiplicity, correction factors (w_i) are computed at lower jet p_T thresholds, based on a double ratio between data and MC at different jet multiplicities. The CRs used to calculate the correction factors use the same selection on the variable C as in the associated SR, however the jet p_T threshold is reduced to 60 GeV, to avoid eventual signal contamination. The correction factors are then calculated using the CRs with jet multiplicities $n_{jets} = 4$, and ≥ 7. The SRs are inclusive in jet multiplicity ($\geq n_{jets}$), and are estimated by summing exclusive jet multiplicities up to $n + 2$.

When introducing the selection on the number of b-tagged jets (n_{b-jets}), as in SR1bj and SR2bj, there is a sizeable contribution from the $t\bar{t}$ SM process, with up to 30% of the total background consisting of $t\bar{t}$. In this case, the N^{MC} terms in Equation 2 are treated as the combined sum of multi-jet and $t\bar{t}$ events. Figure 3 shows two examples of the background method with and without the selection on b-tags. The latter figure also shows the small impact of the correction factors w_i.
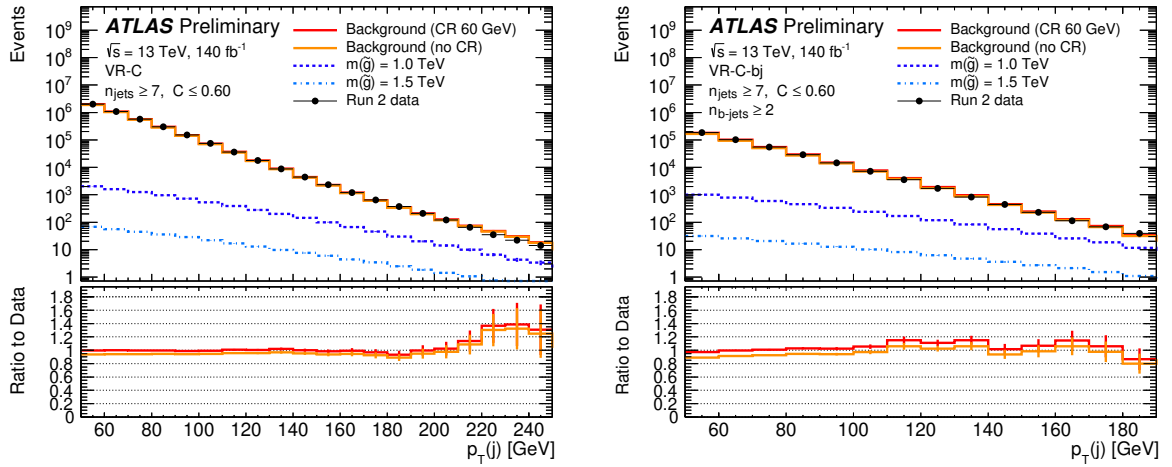
Figure 3: Test of the background method at different jet p_T requirements without (left) and with (right) b-tagging selections. The red line is the prediction using correction factors estimated in the CR, while the orange line is obtained without such corrections.

Background Validation

To evaluate the background modelling several VR sets are defined, presented in Tables 2 and 3. The VRAs and VRBs are designed to validate the method at high values of C, but with lower jet multiplicities to negate signal contamination. The VRCs and VRDs validate the method in a high jet multiplicity and jet momenta region, utilising an inverted C requirement compared to minimise signal contamination. The individual regions in a given VR set are not orthogonal, as the regions only differ in the p_T selection and can therefore be considered to be subsets of each other. Four dedicated VRs (VR-A-bj, VR-B-bj, VR-C-bj and VR-D-bj) are defined to validate the modelling of the selections requiring at least two b-tagged jets, due to the difference in the background composition when b-jets are present in the final state. Figure 3 shows the agreement between the background estimate in the VR-C (left) and VR-C-bj (right) as a function of the jet-p_T threshold used to count the jets. It is seen that there is generally acceptable agreement between the data and the background estimate while increasing the threshold to the highest values used in the SRs. Figure 4 presents the yields of the VRs, displaying the agreement between the background expectation from the jet counting method and the observed data. A slight discrepancy is observed in VR-B3, this

8

non-closure of the method is used to define an additional non-closure uncertainty of 5% on the expected background yields in the SRs.

Table 2: VR definitions and yields, for the regions used to validate the background strategy without an explicit selection on the number of b-tagged jets. The common analysis selections on the H_T, $p_T(j_1)$ and trigger selection are also applied. The uncertainties shown contain both statistical and systematic uncertainties.

	n_{jets}	$p_T(j)$ [GeV]	C	Background Expectation	Data
VR-A1		180	≥ 0.80	73000^{+1800}_{-2400}	70184
VR-A2	5	160	≥ 0.85	65000^{+1800}_{-2200}	64985
VR-A3		150	≥ 0.90	30000^{+2100}_{-1000}	30360
VR-B1		120	≥ 0.80	80000^{+2100}_{-2800}	80271
VR-B2	6	110	≥ 0.85	58000^{+3900}_{-1800}	59997
VR-B3		100	≥ 0.90	28000^{+1000}_{-2000}	30212
VR-C1		180		350^{+37}_{-72}	372
VR-C2	≥ 7	220	≤ 0.60	47^{+6}_{-10}	35
VR-C3		240		18^{+4}_{-3}	14
VR-D1	≥ 8	180	≤ 0.60	23^{+5}_{-6}	16

Table 3: VR definitions and yields, for the regions used to validate the background strategy with a selection on the number of b-tagged jets of ≥ 2. The common analysis selections on the H_T, $p_T(j_1)$ and trigger selection are also applied. The uncertainties shown contain both statistical and systematic uncertainties.

	n_{jets}	$p_T(j)$ [GeV]	C	Background Expectation	Data
VR-A-bj	5	180	≥ 0.85	2100^{+600}_{-100}	1973
VR-B-bj	6	120	≥ 0.85	3700^{+500}_{-300}	3425
VR-C-bj	≥ 7	180	≤ 0.60	34^{+13}_{-6}	39
VR-D-bj	≥ 8	160	≤ 0.60	8^{+6}_{-5}	6

9
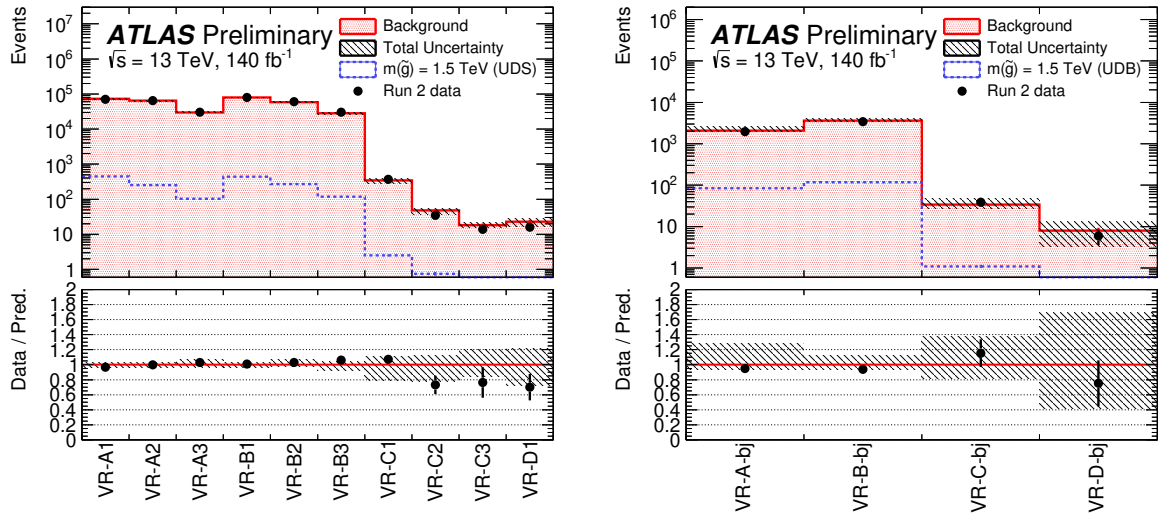
Figure 4: Comparison between the observed data and the background expectation in the VRs. Left: VRs containing no explicit selection on the number of b-tagged jets. Right: VRs containing at least 2 b-tagged jets. The bottom panel presents the ratio of data to the background prediction. The hashed pattern represents the combined statistical and systematic uncertainty on the background estimate.

5.2 Mass resonance analysis

The objective of the mass resonance method is to observe a resonance in the reconstructed candidate gluino mass spectrum. In contrast to the jet counting analysis which could have an excess from a variety of high energy contributions, this search would be an unambigious sign of new physics from resonant production at the probed energy scale. In the case of the direct gluino decay model, the combinatorial issue of correctly identifying which jets should be grouped to each gluino candidate is a significant issue and is the main focus of the method design. A dedicated neural network (NN) is developed which aims to correctly group together the jets from each individual gluino candidate decay. Machine-learning techniques have been applied previously to the combinatorial assignment problem focusing on the reconstruction of standard model processes [51–53] and with less focus on BSM scenarios [54] given the additional unknown of the BSM particle masses. The invariant mass $m_{\tilde{g}}^i$ of the two gluino candidates is built from the jets that are selected by the NN and the average of the two masses $m_{\mathrm{avg}} = \frac{1}{2}\left(m_{\tilde{g}}^1 + m_{\tilde{g}}^2\right)$ is used as the key discriminating variable. The method searches for a localized excess on the m_{avg} spectrum where the background is estimated through a functional fit to a smoothly falling spectrum.

A selection is applied to events entering the mass resonance method requiring at least six jets with p_{T} above 100 GeV, and $C \geq 0.9$. A second selection is defined requiring in addition at least one b-tagged jet, which is used to improve the sensitivity to the UDB model. Further to the previously introduced selections, which are used for the model-dependent interpretation, a set of model-independent SRs are defined using single bins in the invariant mass distribution with a width of 300 GeV, and assume no signal contribution outside of the SR.

Jet assignment model

A NN is built based on the attention mechanism [55], taking inspiration from the transformer model and implemented in PyTorch [56]. The input to the network is the jet four-momentum of the leading eight signal jets, where jets are zero-padded in case the event contains less than eight jets. The first layer consists of an embedding block where each jet is mapped to a latent space. The embedded jets are passed to an encoder block consisting of a jet self-attention block, a gluino-candidate self-attention block, and a jet-candidate cross-attention block. The outputs of the model are three scores per jet representing the probability of the jet to originate from each of the two gluino candidates or a non-signal source such as initial state radiation of pileup. The highest score per jet is used to assign jets in the event to each gluino or non-signal contribution.

The NN is trained using a categorical cross-entropy loss, where the jets are labelled based on $\Delta R < 0.4$ matching with truth partons from the gluino decay. Only events with exactly three jets matched per gluino are used in the training, which represents approximately 50% of the total available events. A tighter preselection, than introduced at the start of this section, is applied to the training set to obtain a sample representative of the final kinematic selections while retaining sufficient statistics, requiring at least six jets with p_{T} above 100 GeV, and $C \geq 0.8$. All the available signal models are used in the training, combining both the UDS and UDB models. The inclusion of all mass points was shown to mitigate the background sculpting by shifting the multijet average mass spectrum to roughly 650 GeV, below the start of the search window at 700 GeV. The model is trained for 500,000 steps with a warm-up phase which increases the learning rate linearly to 10^{-3} during the first 5% of the training steps and is then decayed exponentially.

11
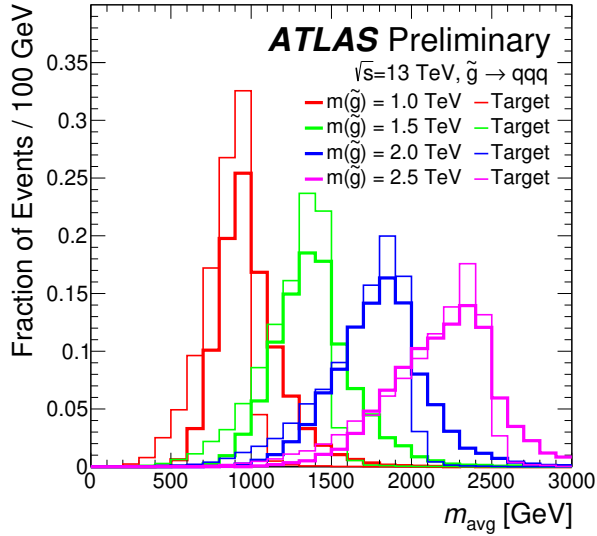
Figure 5: Normalised average mass spectrum comparing the shapes of the reconstructed (solid) and target (light) distributions for different masses. The reconstructed distribution is produced using the NN assignments, whereas the target distribution is built assigning jets to gluinos based on their truth labels.

Hyperparameters were tuned through a population scan and the model with lowest validation loss was retained [57, 58].

The performance of the NN is illustrated in Figure 5. The reconstructed mass matches the target with a small loss in resolution as expected. Target signals show a low-mass tail, especially at higher masses, which originates from the restriction that exactly three jets are matched. This requirement misses additional final state radiation jets which are significant for the highest masses.

Background estimation

Non-resonant QCD processes, which constitute the dominant SM background for this search, result in multijet systems with smoothly-falling invariant mass distributions. In order to estimate this background a parametric function is fit to the observed data distributions, which are binned in 100 GeV-wide bins:

$$f(x) = p_1 (1-x)^{p_2} x^{p_3 + p_4 \ln x}$$

where $x = m_{avg}/\sqrt{s}$ and p_{1-4} are the fitted parameters. This function has been succesfully used in a wide variety of resonance dijet and multijet searches by the CDF, CMS, and ATLAS experiments [59–67]. For the background estimation, a three-parameter fit is used, where p_4 is set to zero, while the four-parameter fit is used to produce pseudodata to validate the fit strategy.

The background distribution is fit using a binned, maximum-likelihood fit implemented using the HistFitter framework [68]. In background-only fits, the signal strength is set to zero, while in the signal-plus-background fits, the signal strength is left as a free parameter. The fit region is set between 0.7 and 3 TeV.
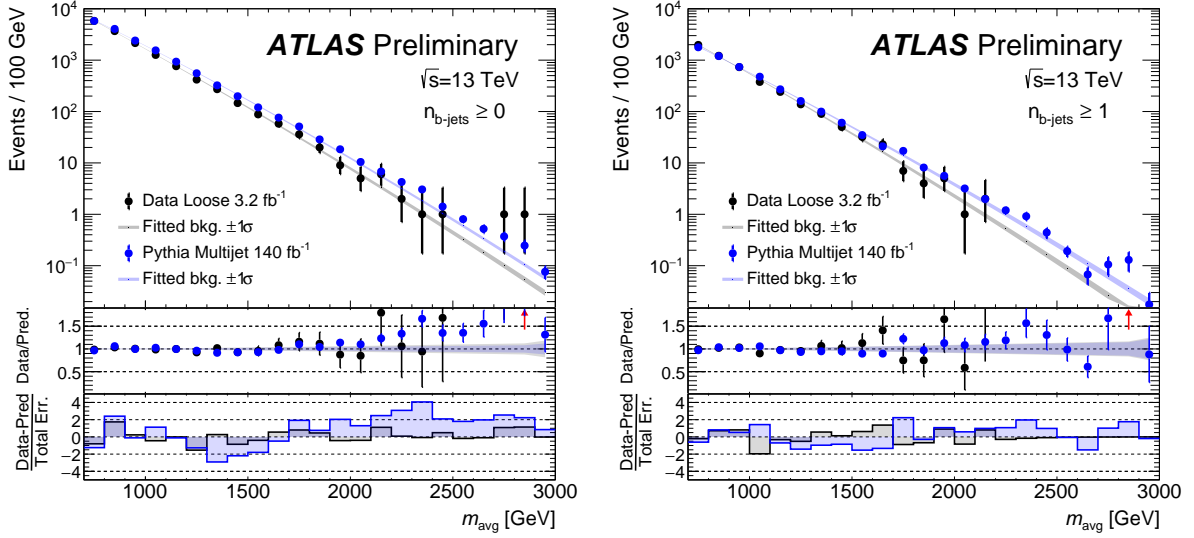
Figure 6: Observed data and fitted background model in the nominal (left) and *b*-tagged (right) regions using a loose selection and 3.2 fb^{-1} of data which matches roughly the number of events expected in the full selection and full dataset. The grey and blue bands present the combined statistical and systematic uncertainty on the background estimate for the data and MC fit functions respectively. The red arrow denotes points which lie above the range of the ratio plot.

The data-driven background fitting procedure was validated with Monte Carlo simulation as well as a small 3.2 fb^{-1} sample of data from 2015 with a loose selection of $C \geq 0.7$ and six jets with p_T above 70 GeV such that the number of events is similar to that of the full dataset with nominal selections. The validity of the background model was tested by checking for a small $\chi^2/N_{\text{D.O.F.}}$ as well as performing 'spurious signal tests' and 'signal injection tests'.

The spurious signal test evaluates whether the fitting procedure is biased in a manner that will produce a non-zero extracted signal when fitting a dataset with no true signal. This test is performed for the nominal 3-parameter fit function by performing a signal-plus-background fit to a pseudodata distribution that is generated from a background-only fit to the data distribution with a 4-parameter function. For each pseudodata distribution, the number of extracted signal events per signal model, n_{spur}, is determined. In order to pass the spurious signal requirement, n_{spur} is required to be less than 20% of the nominal signal events and ratio of the number of spurious signal events to its statistical uncertainty, $n_{\text{spur}}/\sigma(n_{\text{spur}})$ is required to be less than 0.2. The 3-parameter fit function passed the spurious signal test for all signal samples.

The signal injection test is performed to ensure that the background fit is able to extract a signal component with the expected signal strength. Simulated signal models are included together with the background template to form a pseudodata distribution. The injected signals were extracted through the fit to pseudodata and confirmed that the extracted signal strength was in agreement with unity.

Figure 6 shows the validation of the fit model in the 2015 data sample with loose selection and additionally with a multijet MC background sample scaled to 140 fb^{-1}. The fitted function is shown to have acceptable agreement with both the MC and data.

When considering the model-independent SRs the background is estimated through a fit to the reconstructed average mass distribution excluding the signal region bin. This is contrary to the model-dependent fits which are performed using the full average-mass distribution with 100 GeV bins.

6 Systematic Uncertainties

Three categories of systematic uncertainties are considered in both methods: theoretical modelling uncertainties, experimental uncertainties, and uncertainties in the assumptions and methods used for background estimation. The statistical uncertainty due to the limited dataset is the dominant source of uncertainties for both methods all the mass range considered.

Modelling uncertainties related to the simulation of background events arise from missing higher orders in the simulation, PDF and strong coupling constant α_s uncertainties. They are included in the jet counting method as simulation is used to support the background prediction, but not in the mass resonance method. The effect of these uncertainties on the QCD multijet background yields, used to calculate the correction factors in the jet counting analysis, is evaluated through variations of the renormalisation and factorisation scale by factors of two, variations of the shower tune, PDF and α_s parameters within their uncertainties. Additional uncertainties are included on the $t\bar{t}$ background taking the difference between an alternative matrix-element generator (MADGRAPH5_aMC@NLO) and an alternative parton shower (HERWIG 7). The modelling of the QCD multijet background is the leading systematic uncertainty on the jet counting method. In the SRs this uncertainty ranges from roughly 20% up to almost 40% in SR5.

Experimental uncertainties arise from imperfect calibrations and associated uncertainties of the reconstructed objects used in the search. The leading experimental uncertainties arise from the jet energy scale and jet energy resolution. Uncertainties on the pile-up modelling, suppression of pile-up jets, b-tagging efficiencies and mis-tagging rates are included but have a negligible impact on the sensitivity. The impact of experimental uncertainties is also considered for signal samples and correlated with the background variation. The uncertainty in the combined 2015–2018 integrated luminosity is 0.83% [69], obtained using the LUCID-2 detector [70] for the primary luminosity measurements, complemented by measurements using the inner detector and calorimeters.

Dedicated additional uncertainties due the background estimation methodology are included. In the jet counting method the observed level of agreement in the VRs is used to derive an uncertainty due to possible imperfections in the method. The level of disagreement is below one standard deviation in all VRs except for VR-B3. As previously mentioned, an additional non-closure systematic of 5% is added to all SRs with $C > 0.9$, which was derived from the maximum non-closure in the VRs.

In the mass resonance method a spurious signal uncertainty is derived by fitting the distribution obtained from a 4-parameter background fit to a signal plus background hypothesis using the nominal 3-paramater model. The size of the fitted signal is included as uncertainty due to possible limitations of the 3-parameter model to capture the correct background distribution. The uncertainty varies from roughly 300 events for a reconstructed average mass of 900 GeV to 5 events at 2500 GeV. The spurious signal uncertainty is the dominant systematic in the mass resonance method, however the largest uncertainty is the statistical uncertainty from the background prediction.

7 Results and Interpretation

The observed data event yields and the corresponding estimates for the backgrounds in the SRs are shown in Figure 7 for the jet counting and mass resonance analyses. No significant excess of data over the expected event yields is observed in any of the SRs.

(a)

(b)

(c)

(d)
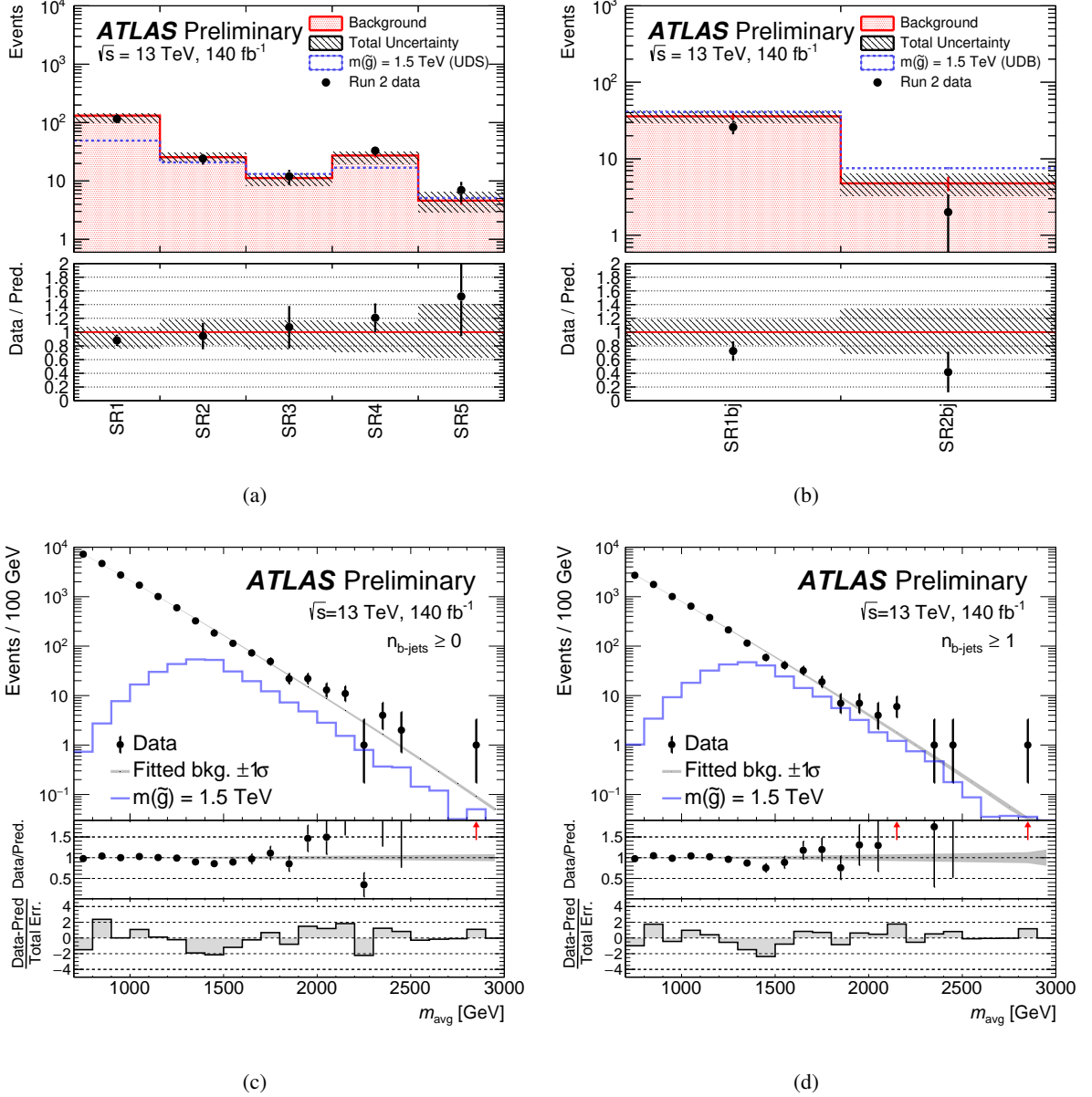
Figure 7: Observed and predicted yields in the signal regions of the jet counting method for the (a) ≥ 0 and (b) ≥ 2 regions. Background only fits to the reconstructed average mass spectrum of the candidate gluinos (c) ≥ 0 and (d) ≥ 1 b-tagged of the mass resonance method. The grey bands include both statistical and systematic uncertainties. The red arrow denotes points which lie above the range of the ratio plot.

The profile likelihood-ratio test [71] is used to establish 95% confidence intervals using the CL_s prescrip-

Signal region	$\langle\epsilon\sigma\rangle^{95}_{obs}$[fb]	S^{95}_{obs}	S^{95}_{exp}	CL_B	$p(s=0)\,(Z)$
SR1	0.32	45	57^{+18}_{-14}	0.51	0.50 (0.00)
SR2	0.09	13	$14.1^{+5.7}_{-4.1}$	0.56	0.50 (0.00)
SR3	0.07	10	$9.5^{+4.1}_{-2.7}$	0.52	0.42 (0.20)
SR4	0.16	22	$17.4^{+6.5}_{-4.7}$	0.26	0.21 (0.79)
SR5	0.07	9.4	$7.4^{+3.6}_{-2.4}$	0.42	0.32 (0.46)
SR1bj	0.08	11	$17.0^{+6.9}_{-4.8}$	0.55	0.50 (0.00)
SR2bj	0.03	4.4	$6.6^{+2.9}_{-1.9}$	0.66	0.50 (0.00)

Table 4: The upper limit table for the signal regions for the jet counting method. Left to right: 95% CL upper limits on the visible cross section ($\langle\epsilon\sigma\rangle^{95}_{obs}$) and on the number of signal events (S^{95}_{obs}). The third column (S^{95}_{exp}) shows the 95% CL upper limit on the number of signal events, given the expected number (and $\pm1\sigma$ excursions on the expectation) of background events. The last two columns indicate the CL_B value, i.e. the confidence level observed for the background-only hypothesis, and the discovery p-value ($p(s=0)$).

tion [72]. The asymptotic approximation of the CL$_s$ is used for all statistical tests except for the high mass model independent bins of the mass resonance method where the number of events is small and toys are generated. The approximation is validated for other regions with moderately small yields for both methods using toys. The uncertainties introduced in the previous section are included as nuisance parameters described by a Gaussian distribution. Upper limits on the product of cross-section, acceptance, and efficiency are shown in Table 4 for the jet counting analysis, and Tables 5 and 6 for the mass resonance analysis. The upper limits range from 7.9 to 0.03 fb, depending on the signal region considered.

Exclusion limits as a function of the masses of the SUSY particles are shown in Figures 8 and 9 for the direct and cascade gluino decay models respectively. For the jet counting analysis, the SR which provides the best expected sensitivity for a given gluino mass is used to set the limit. Gluinos with masses up to 1730 and 1800 GeV are excluded in the direct-decay models where the gluinos decay with 100% BR into qqq (UDS coupling) and qqb (UDB coupling), respectively. For the cascade decay model the limits are provided exclusively by the jet counting approach, where again the SR with the best expected sensitivity to a given signal mass scenario is used to set the limit. Gluinos with masses up to 2230 (2340) GeV are excluded for a neutralino with 1250 GeV mass and UDS (UDB) coupling .

m_{avg} range [GeV]	$\langle\epsilon\sigma\rangle^{95}_{obs}$ [fb]	S^{95}_{obs}	S^{95}_{exp}	CL_B	$p(s=0)\ (Z)$
700 - 1000	7.3	1000	1300^{+460}_{-300}	0.22	0.50 (0.00)
800 - 1100	5.7	800	360^{+150}_{-49}	0.99	0.01 (2.5)
900 - 1200	2.1	290	210^{+88}_{-25}	0.81	0.18 (0.91)
1000 - 1300	1.5	210	160^{+50}_{-34}	0.80	0.18 (0.90)
1100 - 1400	0.54	76	120^{+45}_{-30}	0.09	0.50 (0.00)
1200 - 1500	0.27	37	85^{+33}_{-24}	0.00	0.50 (0.00)
1300 - 1600	0.16	23	63^{+37}_{-18}	0.00	0.50 (0.00)
1400 - 1700	0.16	22	47^{+19}_{-13}	0.00	0.50 (0.00)
1500 - 1800	0.24	33	$38.8^{+16}_{-9.9}$	0.25	0.50 (0.00)
1600 - 1900	0.26	37	$37.9^{+15}_{-9.7}$	0.47	0.50 (0.00)
1700 - 2000	0.30	42	$34.1^{+12}_{-6.8}$	0.71	0.29 (0.55)
1800 - 2100	0.25	35	$28.2^{+12}_{-7.6}$	0.72	0.28 (0.57)
1900 - 2200	0.29	41	$24.5^{+11}_{-3.8}$	0.93	0.06 (1.5)
2000 - 2300	0.19	27	$21.5^{+7.6}_{-4.4}$	0.78	0.19 (0.89)
2100 - 2400	0.15	21	$15.5^{+6.2}_{-2.3}$	0.74	0.20 (0.84)
2200 - 2500	0.08	11	$10.5^{+3.2}_{-1.9}$	0.57	0.40 (0.26)
2300 - 2600	0.08	11	$9.2^{+3.9}_{-1.2}$	0.66	0.27 (0.61)
2400 - 2700	0.05	6.9	$6.8^{+2.1}_{-1.4}$	0.51	0.48 (0.05)
2500 - 2800	0.02	2.3	$3.1^{+2.1}_{-1.2}$	0.26	0.50 (0.01)
2600 - 2900	0.04	5.3	$5.2^{+2.2}_{-1.3}$	0.52	0.46 (0.10)
2700 - 3000	0.06	8.3	$8.2^{+0.4}_{-0.7}$	0.53	0.44 (0.16)

Table 5: The upper limit table for the ≥ 0 b-tagged jets region. Left to right: 95% CL upper limits on the visible cross section ($\langle\epsilon\sigma\rangle^{95}_{obs}$) and on the number of signal events (S^{95}_{obs}). The third column (S^{95}_{exp}) shows the 95% CL upper limit on the number of signal events, given the expected number (and $\pm 1\sigma$ excursions on the expectation) of background events. The last two columns indicate the CL_B value, i.e. the confidence level observed for the background-only hypothesis, and the discovery p-value ($p(s=0)$).

m_{avg} range [GeV]	$\langle\epsilon\sigma\rangle^{95}_{obs}$ [fb]	S^{95}_{obs}	S^{95}_{exp}	CL_B	$p(s=0)$ (Z)
700 - 1000	5.7	800	960^{+330}_{-240}	0.31	0.50 (0.00)
800 - 1100	3.3	460	320^{+100}_{-65}	0.89	0.11 (1.2)
900 - 1200	1.1	150	130^{+38}_{-31}	0.74	0.24 (0.71)
1000 - 1300	0.92	130	92^{+40}_{-13}	0.81	0.18 (0.91)
1100 - 1400	0.36	51	70^{+27}_{-20}	0.17	0.50 (0.00)
1200 - 1500	0.16	23	52^{+21}_{-15}	0.00	0.50 (0.00)
1300 - 1600	0.11	16	39^{+15}_{-11}	0.00	0.50 (0.00)
1400 - 1700	0.12	17	$28.9^{+12}_{-8.1}$	0.04	0.50 (0.00)
1500 - 1800	0.20	27	$24.9^{+25}_{-7.1}$	0.61	0.38 (0.29)
1600 - 1900	0.25	35	$30.0^{+10}_{-7.1}$	0.68	0.45 (0.13)
1700 - 2000	0.21	30	$27.7^{+10}_{-7.7}$	0.58	0.42 (0.20)
1800 - 2100	0.17	24	$24.0^{+5.9}_{-6.2}$	0.51	0.49 (0.03)
1900 - 2200	0.18	25	$21.6^{+5.9}_{-5.8}$	0.71	0.26 (0.65)
2000 - 2300	0.13	18	$17.1^{+5.3}_{-2.1}$	0.63	0.32 (0.47)
2100 - 2400	0.10	13	$12.4^{+3.3}_{-2.6}$	0.63	0.30 (0.51)
2200 - 2500	0.05	6.4	$6.4^{+2.5}_{-1.5}$	0.50	0.50 (0.00)
2300 - 2600	0.05	6.8	$6.7^{+2.6}_{-0.8}$	0.54	0.42 (0.20)
2400 - 2700	0.03	4.0	$3.9^{+2.2}_{-1.2}$	0.52	0.45 (0.14)
2500 - 2800	0.01	2.0	$2.1^{+1.8}_{-0.9}$	0.47	0.49 (0.02)
2600 - 2900	0.04	5.4	$5.3^{+2.2}_{-1.3}$	0.53	0.43 (0.19)
2700 - 3000	0.04	6.1	$6.0^{+2.3}_{-0.6}$	0.53	0.42 (0.20)

Table 6: The upper limit table for the ≥ 1 b-tagged jets region. Left to right: 95% CL upper limits on the visible cross section ($\langle\epsilon\sigma\rangle^{95}_{obs}$) and on the number of signal events (S^{95}_{obs}). The third column (S^{95}_{exp}) shows the 95% CL upper limit on the number of signal events, given the expected number (and $\pm 1\sigma$ excursions on the expectation) of background events. The last two columns indicate the CL_B value, i.e. the confidence level observed for the background-only hypothesis, and the discovery p-value ($p(s=0)$).

(a)

(b)

(c)

(d)
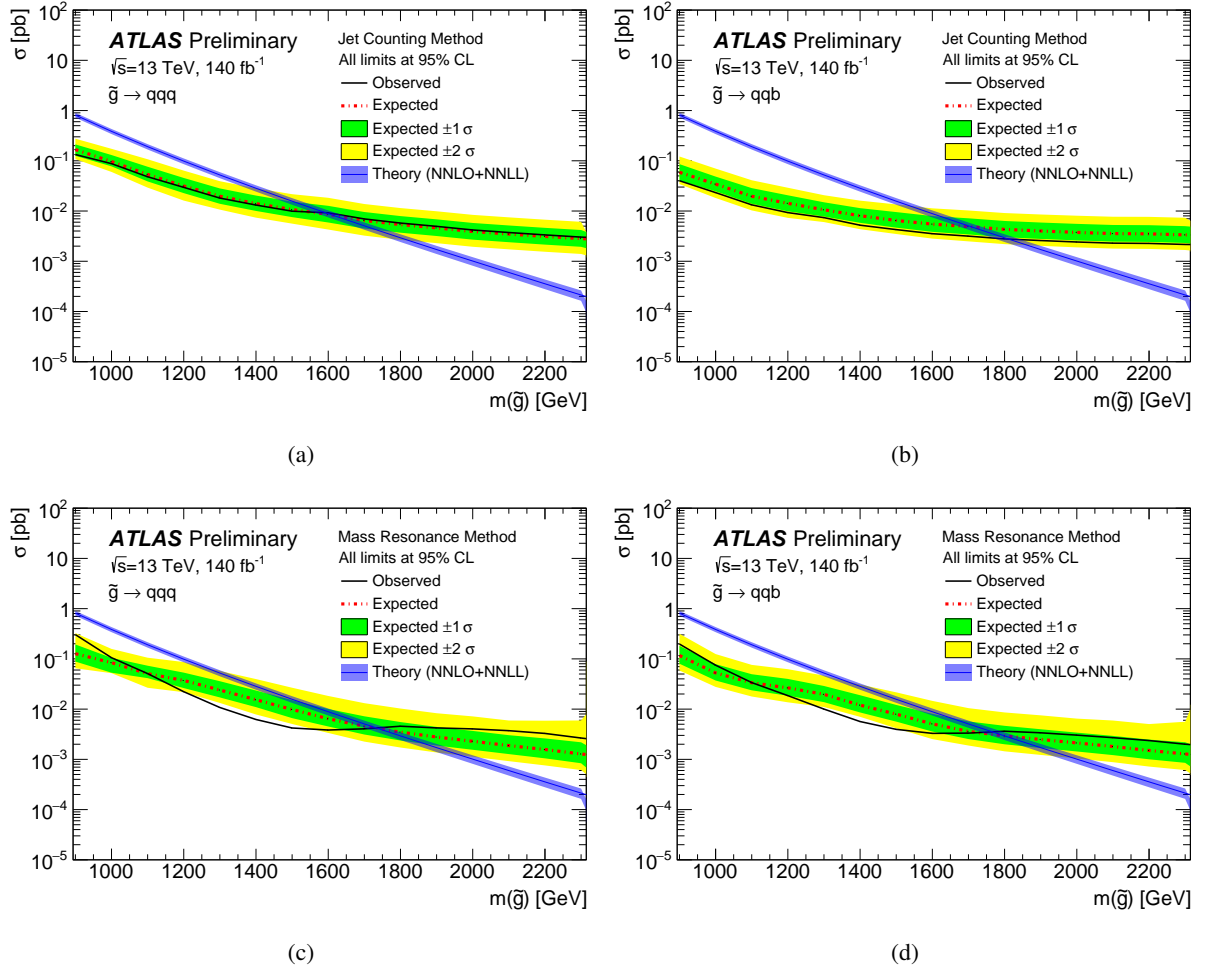
Figure 8: Observed and expected exclusion contours for the gluino direct decay model with (left) UDS and (right) UDB decays, as obtained by the jet counting analysis (top) and mass resonance analysis (bottom). The yellow and green contours of the band around the expected limit are the $\pm1\sigma$ and $\pm2\sigma$ variations including both systematic and statistical uncertainties, respectively. The theoretical prediction is also shown, with the uncertainties in the prediction shown as a coloured band.
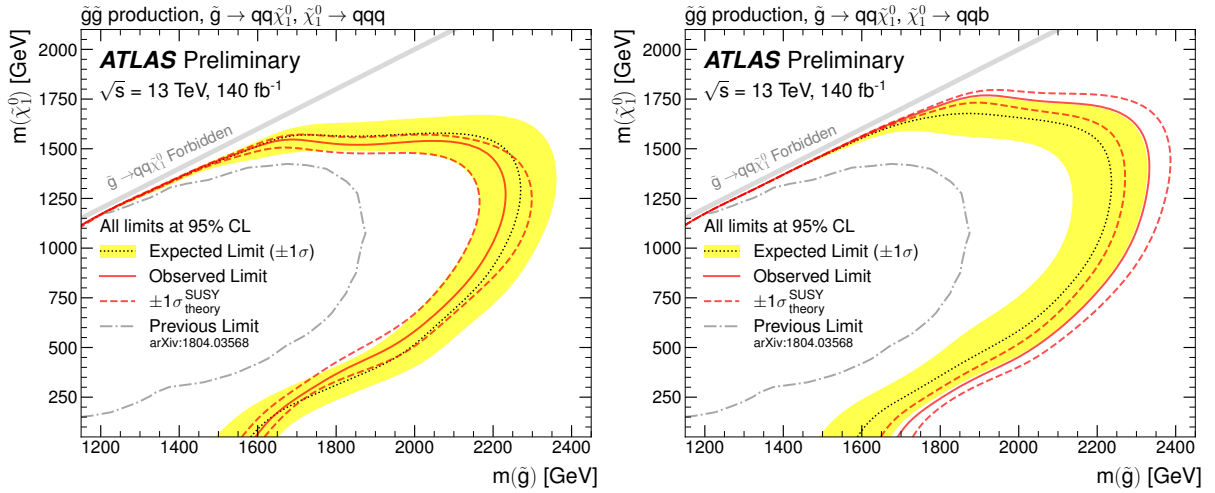
Figure 9: Observed and expected exclusion contours for the gluino cascade decay model with (left) UDS and (right) UDB decays using the Jet Counting method. The contours of the band around the expected limit are the $\pm 1\sigma$ variations, including all uncertainties. The dotted lines around the observed limit illustrate the change in the observed limit as the nominal signal cross-section is scaled up and down by the theoretical uncertainty. The diagonal line indicates the kinematic limit for the decay of the gluino.

8 Conclusion

A search for R-parity-violating SUSY signals in events with multiple jets is performed with 140 fb^{-1} of proton–proton collision data at $\sqrt{s}$ = 13 TeV collected by the ATLAS detector at the LHC. Two methods are utilised, a jet counting method searching for excess events in single-bin signal regions defined at high jet multiplicity and high C, and a mass resonance approach, which searches for a localized excess in the reconstructed gluino mass spectrum. A novel machine-learning approach is employed to address the combinatorial assignment problem and successfully reconstruct the gluino mass. No significant excess is seen in any signal region. Limits are set on the production of gluinos in the gluino direct decay and cascade decay models in $U\bar{D}\bar{D}$ scenarios of RPV SUSY. In the gluino direct decay model, gluinos with masses up to 1800 GeV are excluded at 95% CL. In the gluino cascade decay model, gluinos with masses as high as 2340 GeV are excluded for a neutralino with 1250 GeV mass. Model-independent limits are also set on the signal production cross section times branching ratio in five overlapping signal regions. This search significantly extends the limits from previous results beyond the expected improvement due to the larger dataset. These results improve upon the previously existing LHC limits owing to the larger luminosity, the introduction of event shape variables to suppress background, and the development of machine-learning techniques to assign jets to gluinos and reconstruct their mass.

Acknowledgements

References

[1] Y. Golfand and E. Likhtman,
Extension of the Algebra of Poincare Group Generators and Violation of P Invariance,
JETP Lett. **13** (1971) 323, [Pisma Zh. Eksp. Teor. Fiz. **13** (1971) 452].

[2] D. Volkov and V. Akulov, *Is the neutrino a goldstone particle?*, Phys. Lett. B **46** (1973) 109.

[3] J. Wess and B. Zumino, *Supergauge transformations in four dimensions*,
Nucl. Phys. B **70** (1974) 39.

[4] J. Wess and B. Zumino, *Supergauge invariant extension of quantum electrodynamics*,
Nucl. Phys. B **78** (1974) 1.

[5] S. Ferrara and B. Zumino, *Supergauge invariant Yang-Mills theories*, Nucl. Phys. B **79** (1974) 413.

[6] A. Salam and J. Strathdee, *Super-symmetry and non-Abelian gauges*, Phys. Lett. B **51** (1974) 353.

[7] N. Sakai, *Naturalness in supersymmetric GUTS*, Z. Phys. C **11** (1981) 153.

[8] S. Dimopoulos, S. Raby, and F. Wilczek, *Supersymmetry and the scale of unification*,
Phys. Rev. D **24** (1981) 1681.

[9] L. E. Ibáñez and G. G. Ross, *Low-energy predictions in supersymmetric grand unified theories*,
Phys. Lett. B **105** (1981) 439.

[10] S. Dimopoulos and H. Georgi, *Softly broken supersymmetry and SU(5)*,
Nucl. Phys. B **193** (1981) 150.

[11] G. R. Farrar and P. Fayet, *Phenomenology of the production, decay, and detection of new hadronic
states associated with supersymmetry*, Phys. Lett. B **76** (1978) 575.

[12] H. Goldberg, *Constraint on the Photino Mass from Cosmology*, Phys. Rev. Lett. **50** (1983) 1419,
Erratum: Phys. Rev. Lett. **103** (2009) 099905.

[13] J. Ellis, J. Hagelin, D. V. Nanopoulos, K. A. Olive, and M. Srednicki,
Supersymmetric relics from the big bang, Nucl. Phys. B **238** (1984) 453.

[14] J. A. Evans, Y. Kats, D. Shih, and M. J. Strassler,
Toward Full LHC Coverage of Natural Supersymmetry, JHEP **07** (2014) 101,
arXiv: `1310.5758 [hep-ph]`.

[15] B. Batell, T. Lin, and L.-T. Wang, *Flavored Dark Matter and R-Parity Violation*,
JHEP **01** (2014) 075, arXiv: `1309.4462 [hep-ph]`.

[16] G. D'Ambrosio, G. F. Giudice, G. Isidori, and A. Strumia,
Minimal Flavour Violation: an effective field theory approach, Nucl. Phys. B **645** (2002) 155,
arXiv: `hep-ph/0207036`.

[17] C. Csáki, Y. Grossman, and B. Heidenreich, *MFV SUSY: A Natural Theory for R-Parity Violation*,
Phys. Rev. D **85** (2012) 095009, arXiv: `1111.1239 [hep-ph]`.

[18] J. Alwall, M.-P. Le, M. Lisanti, and J. G. Wacker,
Searching for directly decaying gluinos at the Tevatron, Phys. Lett. B **666** (2008) 34,
arXiv: `0803.0019 [hep-ph]`.

[19] J. Alwall, P. Schuster, and N. Toro,
Simplified models for a first characterization of new physics at the LHC,
Phys. Rev. D **79** (2009) 075020, arXiv: `0810.3921 [hep-ph]`.

[20] D. Alves et al., *Simplified models for LHC new physics searches*, J. Phys. G **39** (2012) 105005, arXiv: 1105.2838 [hep-ph].

[21] ATLAS Collaboration, *Search for massive supersymmetric particles decaying to many jets using the ATLAS detector in pp collisions at $\sqrt{s}$ = 8 TeV*, Phys. Rev. D **91** (2015) 112016, arXiv: 1502.05686 [hep-ex], Erratum: Phys. Rev. D **93** (2016) 039901.

[22] ATLAS Collaboration, *Search for R-parity-violating supersymmetric particles in multi-jet final states produced in pp collisions at $\sqrt{s}$ = 13 TeV using the ATLAS detector at the LHC*, Phys. Lett. B **785** (2018) 136, arXiv: 1804.03568 [hep-ex].

[23] CMS Collaboration, *Search for pair-produced three-jet resonances in proton–proton collisions at $\sqrt{s}$ = 13 TeV*, Phys. Rev. D **99** (2019) 012010, arXiv: 1810.10092 [hep-ex].

[24] ATLAS Collaboration, *The ATLAS Experiment at the CERN Large Hadron Collider*, JINST **3** (2008) S08003.

[25] ATLAS Collaboration, *The ATLAS Collaboration Software and Firmware*, ATL-SOFT-PUB-2021-001, 2021, URL: https://cds.cern.ch/record/2767187.

[26] ATLAS Collaboration, *ATLAS data quality operations and performance for 2015-2018 data-taking*, JINST **15** (2020) P04003, arXiv: 1911.04632 [physics.ins-det].

[27] J. Alwall, M. Herquet, F. Maltoni, O. Mattelaer, and T. Stelzer, *MadGraph 5 : Going Beyond*, JHEP **06** (2011) 128, arXiv: 1106.0522 [hep-ph].

[28] S. Mrenna and P. Skands, *Automated parton-shower variations in PYTHIA 8*, Phys. Rev. D **94** (2016) 074005, arXiv: 1605.08352 [hep-ph].

[29] ATLAS Collaboration, *ATLAS Pythia 8 tunes to 7 TeV data*, ATL-PHYS-PUB-2014-021, 2014, URL: https://cds.cern.ch/record/1966419.

[30] NNPDF Collaboration, R. D. Ball, et al., *Parton distributions with LHC data*, Nucl. Phys. B **867** (2013) 244, arXiv: 1207.1303 [hep-ph].

[31] D. J. Lange, *The EvtGen particle decay simulation package*, Nucl. Instrum. Meth. A **462** (2001) 152.

[32] S. Agostinelli et al., *Geant4 – a simulation toolkit*, Nucl. Instrum. Meth. A **506** (2003) 250.

[33] A. Ribon et al., *Status of Geant4 hadronic physics for the simulation of LHC experiments at the start of the LHC physics program*, (2010), URL: https://lcgapp.cern.ch/project/docs/noteStatusHadronic2010.pdf.

[34] T. Sjöstrand et al., *An introduction to PYTHIA 8.2*, Comput. Phys. Commun. **191** (2015) 159, arXiv: 1410.3012 [hep-ph].

[35] S. Alioli, P. Nason, C. Oleari, and E. Re, *A general framework for implementing NLO calculations in shower Monte Carlo programs: the POWHEG BOX*, JHEP **06** (2010) 043, arXiv: 1002.2581 [hep-ph].

[36] H. B. Hartanto, B. Jäger, L. Reina, and D. Wackeroth, *Higgs boson production in association with top quarks in the POWHEG BOX*, Phys. Rev. D **91** (2015) 094003, arXiv: 1501.04498 [hep-ph].

[37] M. Bähr et al., *Herwig++ physics and manual*, Eur. Phys. J. C **58** (2008) 639, arXiv: 0803.0883 [hep-ph].

[38] J. Bellm et al., *Herwig 7.0/Herwig++ 3.0 release note*, Eur. Phys. J. C **76** (2016) 196, arXiv: 1512.01178 [hep-ph].

[39] T. Sjöstrand, S. Mrenna, and P. Skands, *A brief introduction to PYTHIA 8.1*, Comput. Phys. Commun. **178** (2008) 852, arXiv: 0710.3820 [hep-ph].

[40] ATLAS Collaboration, *The Pythia 8 A3 tune description of ATLAS minimum bias and inelastic measurements incorporating the Donnachie–Landshoff diffractive model*, ATL-PHYS-PUB-2016-017, 2016, URL: https://cds.cern.ch/record/2206965.

[41] ATLAS Collaboration, *Measurement of the Inelastic Proton–Proton Cross Section at $\sqrt{s} = 13\,TeV$ with the ATLAS Detector at the LHC*, Phys. Rev. Lett. **117** (2016) 182002, arXiv: 1606.02625 [hep-ex].

[42] ATLAS Collaboration, *Jet reconstruction and performance using particle flow with the ATLAS Detector*, Eur. Phys. J. C **77** (2017) 466, arXiv: 1703.10485 [hep-ex].

[43] M. Cacciari, G. P. Salam, and G. Soyez, *The anti-k_t jet clustering algorithm*, JHEP **04** (2008) 063, arXiv: 0802.1189 [hep-ph].

[44] ATLAS Collaboration, *Performance of pile-up mitigation techniques for jets in pp collisions at $\sqrt{s} = 8\,TeV$ using the ATLAS detector*, Eur. Phys. J. C **76** (2016) 581, arXiv: 1510.03823 [hep-ex].

[45] ATLAS Collaboration, *Identification and energy calibration of hadronically decaying tau leptons with the ATLAS experiment in pp collisions at $\sqrt{s} = 8\,TeV$*, Eur. Phys. J. C **75** (2015) 303, arXiv: 1412.7086 [hep-ex].

[46] ATLAS Collaboration, *Electron and photon performance measurements with the ATLAS detector using the 2015–2017 LHC proton–proton collision data*, JINST **14** (2019) P12006, arXiv: 1908.00005 [hep-ex].

[47] ATLAS Collaboration, *Electron reconstruction and identification in the ATLAS experiment using the 2015 and 2016 LHC proton–proton collision data at $\sqrt{s} = 13\,TeV$*, Eur. Phys. J. C **79** (2019) 639, arXiv: 1902.04655 [hep-ex].

[48] ATLAS Collaboration, *Muon reconstruction performance of the ATLAS detector in proton–proton collision data at $\sqrt{s} = 13\,TeV$*, Eur. Phys. J. C **76** (2016) 292, arXiv: 1603.05598 [hep-ex].

[49] ATLAS Collaboration, *Measurement of hadronic event shapes in high-p_T multijet final states at $\sqrt{s} = 13\,TeV$ with the ATLAS detector*, JHEP **01** (2021) 188, [Erratum: JHEP 12, 053 (2021)], arXiv: 2007.12600 [hep-ex].

[50] ATLAS Collaboration, *Search for pair production of massive particles decaying into three quarks with the ATLAS detector in $\sqrt{s} = 7\,TeV$ pp collisions at the LHC*, JHEP **12** (2012) 086, arXiv: 1210.4813 [hep-ex].

[51] A. Shmakov et al., *SPANet: Generalized permutationless set assignment for particle physics using symmetry preserving attention*, SciPost Phys. **12** (2022) 178, URL: https://scipost.org/10.21468/SciPostPhys.12.5.178.

[52] S. Qiu, S. Han, X. Ju, B. Nachman, and H. Wang, *A Holistic Approach to Predicting Top Quark Kinematic Properties with the Covariant Particle Transformer*, 2023, arXiv: 2203.05687 [hep-ph].

[53] L. Ehrke, J. A. Raine, K. Zoch, M. Guth, and T. Golling,
Topological Reconstruction of Particle Physics Processes using Graph Neural Networks, 2023,
arXiv: 2303.13937 [hep-ph].

[54] A. Badea et al., *Solving combinatorial problems at particle colliders using machine learning*,
Phys. Rev. D **106** (1 2022) 016001,
URL: https://link.aps.org/doi/10.1103/PhysRevD.106.016001.

[55] A. Vaswani et al., *Attention Is All You Need*, 2017, arXiv: 1706.03762 [cs.CL].

[56] A. Paszke et al., *PyTorch: An Imperative Style, High-Performance Deep Learning Library*, 2019,
arXiv: 1912.01703 [cs.LG].

[57] M. Jaderberg et al., *Population Based Training of Neural Networks*, 2017,
arXiv: 1711.09846 [cs.LG].

[58] R. Liaw et al., *Tune: A Research Platform for Distributed Model Selection and Training*,
arXiv preprint arXiv:1807.05118 (2018).

[59] T. Aaltonen et al.,
Search for new particles decaying into dijets in proton-antiproton collisions at s**(1/2) = 1.96-TeV,
Phys. Rev. D **79** (2009) 112002, arXiv: 0812.4036 [hep-ex].

[60] ATLAS Collaboration, *Search for New Particles in Two-Jet Final States in 7 TeV Proton–Proton
Collisions with the ATLAS Detector at the LHC*, Phys. Rev. Lett. **105** (2010) 161801,
arXiv: 1008.2461 [hep-ex].

[61] CMS Collaboration,
Search for Resonances in the Dijet Mass Spectrum from 7 TeV pp Collisions at CMS,
Phys. Lett. B **704** (2011) 123, arXiv: 1107.4771 [hep-ex].

[62] ATLAS Collaboration, *Search for new phenomena in the dijet mass distribution using pp collision
data at $\sqrt{s} = 8$ TeV with the ATLAS detector*, Phys. Rev. D **91** (2015) 052007,
arXiv: 1407.1376 [hep-ex].

[63] ATLAS Collaboration, *Search for new phenomena in dijet mass and angular distributions from pp
collisions at $\sqrt{s} = 13$ TeV with the ATLAS detector*, Phys. Lett. B **754** (2016) 302,
arXiv: 1512.01530 [hep-ex].

[64] CMS Collaboration, *Search for dijet resonances in proton–proton collisions at $\sqrt{s} = 13$ TeV and
constraints on dark matter and other models*, Phys. Lett. B **769** (2017) 520,
arXiv: 1611.03568 [hep-ex].

[65] ATLAS Collaboration,
*Search for new phenomena in multi-body invariant masses in events with at least one isolated lepton
and two jets using $\sqrt{s} = 13$ TeV proton–proton collision data collected by the ATLAS detector*,
(2022), arXiv: 2211.08945 [hep-ex].

[66] ATLAS Collaboration, *Search for new resonances in mass distributions of jet pairs using $139\,fb^{-1}$
of pp collisions at $\sqrt{s} = 13$ TeV with the ATLAS detector*, JHEP **03** (2020) 145,
arXiv: 1910.08447 [hep-ex].

[67] CMS Collaboration, *Search for resonant and nonresonant production of pairs of dijet resonances in
proton–proton collisions at $\sqrt{s} = 13$ TeV*, (2022), arXiv: 2206.09997 [hep-ex].

[68] M. Baak et al., *HistFitter software framework for statistical data analysis*,
Eur. Phys. J. C **75** (2015) 153, arXiv: 1410.1280 [hep-ex].

[69] ATLAS Collaboration,
Luminosity determination in pp collisions at $\sqrt{s} = 13$ TeV using the ATLAS detector at the LHC,
(2022), arXiv: `2212.09379 [hep-ex]`.

[70] G. Avoni et al., *The new LUCID-2 detector for luminosity measurement and monitoring in ATLAS*,
JINST **13** (2018) P07017.

[71] G. Cowan, K. Cranmer, E. Gross, and O. Vitells,
Asymptotic formulae for likelihood-based tests of new physics, Eur. Phys. J. C **71** (2011) 1554,
arXiv: `1007.1727 [physics.data-an]`, Erratum: Eur. Phys. J. C **73** (2013) 2501.

[72] A. L. Read, *Presentation of search results: the CL_S technique*, J. Phys. G **28** (2002) 2693.

[73] ATLAS Collaboration, *ATLAS Computing Acknowledgements*, ATL-SOFT-PUB-2021-003, 2021,
URL: `https://cds.cern.ch/record/2776662`.